Macalester Journal of Physics and Astronomy

Volume 5
Issue 1 *Spring 2017*

Article 1

May 2017

A Direct Comparison of Lyman-Alpha and Neutral Hydrogen Morphologies

Kathleen Fitzgibbon
Macalester College, kfitzgib@macalester.edu

John M. Cannon
Macalester College, jcannon@macalester.edu

A Direct Comparison of Lyman-Alpha and Neutral Hydrogen Morphologies

Abstract

The Lyman-Alpha Reference Sample (LARS) and its extension (eLARS) represent an exhaustive campaign to reverse-engineer galaxies. The main goal is to understand how \lya radiation is transported within galaxies: what fraction of it escapes, and what physical properties affect the \lya morphology and radiative transport (e.g., dust and gas content, metallicity, kinematics, properties of the producing and underlying stellar populations). Two galaxies from the sample, LARS02 and LARS09, were observed using the B and C configurations of the Very Large Array to examine the neutral hydrogen emission, which can be used to determine a galaxy's neutral hydrogen (HI) structure and kinematics. Images of the \HI mass surface density and of the intensity weighted \HI velocity field were created at angular scales of $\sim$8 arcseconds, which corresponds to $\sim$5 kpc for LARS02 and $\sim$8 kpc for LARS09. Extended \HI gas is detected at high significance up to $\sim$30 kpc from the optical body of LARS02. LARS09 has a severely disturbed optical morphology; our new \HI observations reveal that LARS09 is interacting with the nearby field galaxy SDSS J082353.65+280622.2. By combining these moment maps with direct imaging of the \lya morphology from the Hubble Space Telescope, this program has produced the first direct comparison of \lya and \HI morphologies. These observations demonstrate concept for a significant observational campaign to produce similar comparisons in the remaining 40 LARS and eLARS galaxies.

Keywords

galaxies: individual (LARS02, LARS09), dust, extinction, galaxies: evolution, galaxies: luminosity function, mass function, galaxies: star formation

1. Introduction

The Lyman-alpha emission line (Lyα) at 1216 Å is a unique and powerful diagnostic probe of the high-redshift z universe. Lyα photons are produced as UV photons emerging from hot stars and travel through the surrounding material of the galaxy. These photons are reprocessed into a single narrow feature, forming the most intrinsically luminous emission line in hot sources. This also makes it the primary diagnostic for identifying the highest redshift galaxies, due to its ultraviolet rest wavelength and its intrinsic power, reprocessing around one-third of the ionizing energy into a single spectral feature (see, e.g., Hayes et al. 2010 and references therein). This makes Lyα emission more accessible to spot and to trace than many other spectral features. Additionally, at such high redshifts, the emission line can potentially bestow spectroscopic confirmation of distant galaxies chosen by other methods (e.g., Stark et al. 2010).

Lyα is a resonance line, meaning wherever the photons encounter neutral hydrogen atoms, they scatter with equal energy but in random directions. This may occur in the interstellar medium (ISM) of the galaxies themselves, or in the circumgalactic medium (CGM) that immediately surrounds them. Therefore, this scattering reveals information not only about the nebula in which the photon was produced, but also about any media the photons may have traveled through. This scattering can result in extended Lyα structures such as those found in Lyα emitters (LAE) by Steidel et al. (2011) and Zheng et al. (2011), among others. In many LARS galaxies, Lyα emission is prominent on physical scales that exceed those of both the massive stellar populations and the star formation regions that give rise to the Lyα photons; Lyα photons are resonantly scattered to large radii in most of the LARS galaxies. Inside the ISM, Atek et al. (2014) found that the radiative transport of Lyα depends on dust extinction, but this correlation shows large scatter, and there are other factors to consider. The resonant scattering of Lyα is complex, because the visibility of the line is shaped by many factors, including dust content (Charlot & Fall 1993, Verhamme et al. 2008, Atek et al. 2009, Hayes et al. 2010), dust geometry (Scarlata et al. 2009), neutral gas content and kinematics (Kunth et al. 1998, Mas-Hesse et al. 2003, Cannon et al. 2004), and gas geometry (Neufeld 1991, Giavalisco et al. 1996, Hansen & Oh 2006, Laursen et al. 2013, Duval et al. 2014). Given this complexity, it is clear that the mechanisms controlling the total escape fraction of Lyα photons ($f_{\rm esc}^{\rm Ly\alpha}$; defined as the ratio of observed to intrinsic Lyα luminosity, Hayes et al. 2005, 2013), are still inadequately understood. These interconnected radiative transport issues imply that the total escape fraction of Lyα photons cannot be predicted from knowledge of any one of these quantities. Thus, photometric measurements of Lyα will reflect the underlying properties of galaxies only in the very broadest statistical sense. By understanding which factors affect Lyα radiative transport, we can improve realistic models of galactic evolution that include specific treatment of this cosmologically important spectral

line.

The Lyman Alpha Reference Sample (LARS) and its successor, the Extended Lyman Alpha Reference Sample (eLARS), constitute a comprehensive multi-wavelength observational campaign studying star-forming galaxies that is making great strides forward in understanding the physics of this Lyα production and radiative transport. The composite LARS+eLARS sample spans a wide range in UV luminosity and star-formation rates (LARS had an Hα emission equivalent width of W(Hα) $\geq$ 100 Å; eLARS lowered that threshold to W(Hα) $\geq$ 35 Å); this provides a distribution of galaxies that fall along the normal range of star formation rates at both low- and high-z, as well as increasing the statistical significance of any trends observed. A graph of this range in parameter space can be seen in the lower right panel of Fig. 1. More details about the selection process can be found in Östlin et al. (2014) and Hayes et al. (2014), hereafter Papers I and II, respectively. These programs aim to study the conditions under which Lyα photons manage to escape from host galaxies, based on spatially resolved observations of the Lyα emission line. The data required to study Lyα in these galaxies was obtained in Cycle 18 (imaging) and Cycle 19 (spectroscopy) from the Hubble Space Telescope (HST). It is important to note that the galaxies were not selected based on Lyα characteristics, meaning the results can be applied to both high- and low-z star-forming galaxies.

The basic properties of LARS02 and LARS09 can be found in Table 1. A distance of 130 Mpc was derived from the luminosity distance for LARS02 and the same method was used to find a distance of 210 Mpc for LARS09. Using SDSS spectroscopy, these galaxies have redshifts of $z = 0.030$ and $z = 0.047$, respectively. All listed global UV properties were found in Hayes et al. (2014) (see Table 2). LARS02 has much smaller values than LARS09 for stellar mass and star formation rate (SFR), but a much higher Lyα escape fraction and Lyα equivalent width, as well as a slightly higher Lyα luminosity. The two galaxies have comparable metallicity.

In Pardy et al. (2014), hereafter Paper III, we presented a pilot HI study of the neutral ISM in a subset of 5 of the LARS galaxies. Building on those results, here we present new high angular resolution VLA HI imaging of LARS02 and LARS09 and compare the results to HST images of Lyα emission. The goal of this program is to quantify the role that neutral gas morphology and kinematics play in Lyα resonant scattering. *To our knowledge, this work includes the first direct comparisons of the morphologies of HI and Lyα emission on meaningful angular scales.*

2. Observations and Data Reduction

Our observations were obtained using the Karl G. Jansky Very Large Array (VLA) in Socorro, NM in program VLA/14B-044 (PI: Cannon). The C observations were acquired in October and November of 2014 and the B observations were acquired in April and May of 2015. LARS02 was observed in both B and C configuration for a total of approximately 21 hours. LARS09 was observed in both B and C configuration for a total of approximately 18 hours. The spectral window was 1024 channels over 16 MHz of total bandwidth, using a standard WIDAR (Wide-band Interferometric Digital ARchitecture) correlator configuration, resulting in a spectral resolution of 3.3 $\mathrm{km\,s^{-1}ch^{-1}}$.

The data were reduced in CASA using standard prescriptions. The observations were somewhat contaminated with radio frequency interference (RFI), but the RFI was flagged and poor baselines were removed. The quasars J1331+305 (3C286) and J0542+498 (3C147) were used as primary calibrators. The secondary calibrator was J0834+5534 for LARS02 and J0741+3112 for LARS09. The channels not containing the galaxy were UV-continuum-subtracted using a first-order fit. CASA performed on-the-fly imaging of both the six data sets of LARS02 and the seven data sets of LARS09 simultaneously, resulting in one final B+C data set for each galaxy.

After calibration, these data sets were then cleaned to 2.5σ and a channel width of 10 km $\mathrm{s^{-1}}$. We found that the largest beam area per channel was $8.42'' \times 7.42''$ for LARS02 with an rms noise of $\sigma = 0.23$ mJy $\mathrm{Bm^{-1}}$. For LARS09, these values were $11.11'' \times 8.73''$ and $\sigma = 0.23$ mJy $\mathrm{Bm^{-1}}$. LARS02 was then smoothed to a beam size of $8.0'' \times 9.0''$, while LARS09 was smoothed to a beam size of $11.5.'' \times 9.25''$.

Using these smoothed cubes, we created masks by enforcing blanks at the 2σ level, using the rms noise in line-free channels as our σ value, and hand drawing the mask shape over the channels containing the galaxy. Real emission features were identified as those that were spatially coincident across at least two consecutive channels. The corresponding channel maps can be seen in Figures 2 and 3. Our final data cubes were obtained by applying these masks to each original (non-smoothed) cube. By collapsing the final cubes, we created two-dimensional moment zero and moment one maps (HI mass surface density and intensity-weighted velocity field, respectively) for both LARS02 and LARS09, using standard procedures. These moment maps can be seen in Figures 4 and 5. We assume a 10% uncertainty on the overall calibration and absolute flux scale of the VLA images.

HST images were made from Cycle 18 observations (Proposal 12310, PI: Östlin) and from Cycle 19 spectroscopy (Proposal 12583, PI: Hayes) using F336W, F438W, and F775W filters. We then overlaid our HI contours onto these observations to compare the neutral

hydrogen morphologies to optical and Lyα emission morphologies.

3. Discussion

3.1. B+C Configuration Observations

3.1.1. LARS02

LARS02 has the highest global Lyα escape fraction of the original LARS galaxies (0.56) and the highest Lyα /Hα ratio (4.53), but also one of the lowest star formation rates (Pardy et al. 2014). Rivera-Thorsen et al. (2015) found a classic P Cygni-like emission profile in Lyα within the COS aperture. The SiII absorption lines are only slightly blueshifted from LARS02's systemic velocity and are strongly fluorescent, as is the OI. They hypothesized that the low dust content and small velocity range of LARS02 has helped to enlarge its Lyα escape fraction, despite its low outflow velocity and high inferred metal line covering fraction. Within the COS aperture, LARS09 is the strongest absorber in the sample from Rivera-Thorsen et al. (2015), although globally it is a weak Lyα emitter, most likely due to its lack of outflow, wide velocity range, and high inferred column density. Pardy et al. (2014) identified LARS09 as a global Lyα emitter at large scales, where R $>$ 10 kpc, and as either a loose spiral or interacting pair, based on the severely warped optical morphology of LARS09. Rivera-Thorsen et al. (2015) noted that a weak contaminating line was likely affecting the blue wing of SiII 1260 in LARS09, causing it to become deeper.

With the finer angular resolution afforded by the B and C configuration observations, much more detail in the morphology of the HI cloud is revealed. In panel (a) of Fig. 4, the bulk of the gas stretches northeast to southwest, with an arm arcing from the southwest tip back up north and east. This arc begins and ends moderately offset in angular distance from the optical galaxy. The HI halo for LARS02 is much larger than its stellar body, spanning $\sim$60-90$''$($\sim$37.8-56.7 kpc), compared to the optical extending less than 10$''$(6.3 kpc). The highest density of the HI gas is located at approximately the center of the HI mass, which is slightly southwest of the optical part of the galaxy. There is mostly coherent rotation, as the central isovelocity contours in panel (b) of Fig. 4 are parallel to one another, covering a velocity range between 8610 and 8750 km s^{-1}. The southwestern part of the HI gas is mostly located at the same position in velocity space.

The morphology of the Lyα emission follows the optical morphology of the galaxy, extending in a halo. The brightest emission is located at the northern optical end of this galaxy. Overlaying the moment zero map contours onto an HST image of the Lyα emission (Fig. 4,

panel e), we see that in the southwest part of the galaxy the HI column density is highest. Conversely, at the northern end of LARS02, where there is less HI gas, the Lyα emission is brighter.

Pardy et al. (2014) found single-dish and interferometric D configuration HI flux and mass, as can be seen in Table 3. To these numbers we compare our own, derived from interferometric B+C configuration observations. For LARS02, our numbers are closer to those from the single-dish observations, with comparable errors.

3.1.2. LARS09

In Fig. 5, we see that LARS09 actually appears to be interacting with a smaller, dimmer galaxy beside it, SDSS J082353.65+280622.2. Originally, when looking at the optical image, we believed this to be an unrelated background galaxy, but it appears to be at the same redshift as LARS09, based on the agreement of the HI velocities. In panel (a), the two galaxies are clearly sharing gas, and in (b), we see both galaxies rotating towards the same point at the southern end. LARS09 has more HI than the companion galaxy, as can be seen in the moment zero map. The point of highest column density agrees very well with the optical center of LARS09, indicated by the red circle in panel (c) of Fig. 5. The secondary clump of gas also agrees well with the optical center of the secondary galaxy. The bright point at the southern tip of LARS09 is a foreground star and should be ignored. The galaxy itself is slightly oversaturated in our images in order to render visible the smaller, dimmer J082353.65+280622.2. The isovelocity contours in panel (b) seem to agree very well with the interpretation of two coherently rotating galaxies sharing gas at one end. The contours form two sets of parallel lines, one for LARS09 and one for the companion galaxy. At the southern end, these contours turn towards each other to smoothly transition over the shared HI gas. This companion galaxy could be the source of the weak contaminating line found in Rivera-Thorsen et al. (2015). Herenz et al. (2016) also conclude that LARS09 is closely interacting with SDSS J082353.65+280622.2.

The shape of the Lyα emission closely traces the optical shape of the galaxy LARS09, with comparatively higher concentrations of emission at the northern and southern tips of the optical galaxy. The highest HI column density of LARS09 can be found at its optical center, where Lyα emission is dimmest (Fig. 5, panel e). Correspondingly, the edges of the disk, where the HI gas is less dense, are brighter in Lyα emission, especially at the southern end. Herenz et al. (2016) found the Lyα to be absorbed nearly everywhere along the line of sight toward the areas of Hα production, yet LARS09 is still surrounded by a Lyα halo.

Comparing our interferometric B+C configuration observations again with the single-dish and interferometric D configuration HI flux and mass from Pardy et al. (2014) (Table 3), we see these numbers more closely agree with the ones from the interferometric D configuration observations, with comparable errors.

3.2. Radial Profiles

In order to obtain a more quantitative comparison between HI and Lyα emission, we performed a radial profile analysis. We first regridded the HST Lyα image and our HI moment zero map onto the same WCS (World Coordinate System) grid so that we could compare the two on a pixel by pixel basis. Then an appropriate position angle and inclination angle were chosen for each galaxy, using the HI data to determine i. Both of these parameters are crucial to estimating the dynamic mass of a galaxy, as position angle is the angle of the major axis of the galaxy measured counterclockwise to the north celestial pole, and inclination is the angle at which the disk of the galaxy is tilted with respect to the viewer. For example, a galaxy that appears completely edge on to us ($i = 90$) will have a rotational velocity equal to its observed velocity, whereas for smaller inclination angles, they will not be equivalent. We assume an uncertainty of ± 20 degrees on both parameters. Using the Cosmic Origins Spectrograph (COS) pointing as our center (see Rivera-Thorsen et al. 2015), we integrated radially outwards over concentric elliptical annuli. The result compares the surface brightness of Lyα emission to the neutral hydrogen surface density, the normalized plots of which can be seen in Figures 6 and 7. These values are representative, so physical values will be multiplicative of these; for example, the HI surface density magnitude will be in units of $M_\odot\ pc^{-2}$.

In Fig. 6, the curves for LARS02 do not immediately appear to agree with our assertion that the Lyα emission and the HI surface density are inversely correlated. However, this discrepancy can be explained by the difference in position for the local maxima for each quantity. The annuli over which we integrated are centered on a central point in the optical galaxy, which was the same central pointing for the Lyα spectroscopic observations. However, the highest surface density of the neutral hydrogen gas is further south of the galaxy. This means that our annuli cross though the peak of HI density, then move further out to points of lower density, resulting in the shape of the curve in Fig. 6. Unfortunately, we cannot interpret much information from this plot at this time, other than that the Lyα emission is emerging from within regions with significant HI surface densities.

The plot for LARS09 (Fig. 7) more closely resembles our expectations. In this galaxy, the region of highest HI surface density agrees well with the central pointing of the Lyα data;

therefore the two morphologies are more easily directly compared. As the elliptical annuli radiate from the center, they pass from values of high HI surface brightness to lower values, and from low surface brightness Lyα emission to higher values. We see that the galaxy is actually absorbing Lyα photons in the center of the galaxy, where the HI is most dense. The Lyα first transitions from absorption (below the horizontal dashed line) to emission (above the line) at just over 5 kpc away from the chosen center. Assuming $i = 60°$, this radius corresponds to a mass of roughly 14 $M_\odot$ pc^{-2}.

3.3. Comparison to D Configuration Observations

When looking at the D configuration ($\sim 60''$) observations of LARS02 from Pardy et al. (2014) in Fig. 8, the extended nature of the hydrogen gas in the galaxy is evident. However, because the beam size is so large, the shape is smeared out. With the smaller beam size from the B and C observations, we see the area of highest density HI gas is actually somewhat offset from the optical center. Addtionally, whereas before there was a general extension to the northeast, we can now see a more clearly defined arm of HI gas separate from the main body. The finer angular resolution from the B and C configuration observations yields much more detail in the morphology of the HI clouds.

B and C configuration observations of LARS09 also reveal a wealth of finer structure in the HI morphology that was indiscernible in D configuration. Looking at Fig. 9 (from Pardy et al. 2014), the axis of rotation of the HI gas seems to be notably askew from the axis of rotation of the optical galaxy. With the finer angular resolution resulting from the smaller beam size, we can now tell that this results from the concatentation of the rotation of both LARS09 and of its companion. In the D configuration, there also appeared to be some extension of the HI gas to the southeast; however, this does not show up in the B and C observations. This is most likely due to the large beam size of the former, which spread the gas in that direction, and to its higher sensitivity to surface brightness.

3.4. Future Analysis

All 28 of the eLARS galaxies, as well as 4 additional LARS galaxies, have now had D configuration moment maps created (Eisner et al. 2017, Reilly et al. 2017), with 4 non-detections, for a total of 37 out of the 42 total LARS and eLARS galaxies with secure HI masses. Data collection in A configuration was approved for eLARS01 and LARS09 at C priority, resulting in 6 hours on source for eLARS01 and 2 hours for LARS09. There is a

newly approved program calling for ∼300 hours, with ∼25 sources in C configuration and ∼10 sources in B configuration; data acquisition will begin in May 2017. With more LARS and eLARS galaxies observed with finer angular resolution, we will more thoroughly populate our comparisons of HI and Lyα morphologies, and thereby better interpret any correlation between the two.

4. Conclusion

We have presented new VLA HI spectral line imaging of two galaxies in the Lyman Alpha Reference Sample (LARS). These observations have finer angular resolution than the observations made for these two galaxies in previous work for this study. The resultant smaller beam size allows us to see an abundance of morphological detail that we were before unable to discern. These HI morphologies are crucial to better understanding Lyα radiative transport, which in turn helps us hone models of galactic evolution as we obtain a better physical understanding of what regulates galactic Lyα emission. LARS is a local sample to be used as reference for interpretation of high-z galaxies, so a clearer comprehension of these nearer galaxies will greatly assist us with those younger galaxies that are harder to observe.

With the B and C configuration observations, both of the galaxies are well-resolved. We see that the HI gas of LARS02 is aligned along the same axis that we saw in D configuration data, but the arm structure to the north is now well-defined. In LARS09, we find the HI gas aligns well with the optical galaxy. We also find that LARS09 is sharing gas with a smaller, dimmer companion galaxy.

To our knowledge, this work contains the first direct comparison of Lyα emission and HI morphologies at meaningful angular scales. The diffuse and extended Lyα emission appears to favor regions of low HI column density. However, this comparison has currently only been made for two galaxies. Similar high-resolution observations of a larger number of LARS+eLARS galaxies will determine statistically robust trends.

KF was partially supported by a Science Education Award from the Howard Hughes Medical Institute (HHMI) to Macalester College. KF and JMC thank Macalester College for resources provided.

Facilities: VLA, HST.

REFERENCES

Atek, H., Kunth, D., & Schaerer, D. et al. 2009, A&A, 506, L1

Atek, H., Kunth, D., & Schaerer, D. et al. 2014, A&A, 561, A89

Cannon, J. M., Skillman, E. D., & Kunth, D. et al. 2004, ApJ, 608, 768

Charlot, S. & Fall, S. M. 1993, ApJ, 415, 580

Duval, F., Schaerer, D., Östlin, G., & Laursen, P. 2014, A&A, 562, A52

Eisner, B., Reilly, B., & Cannon, J.M., et.al. 2017. AAS229. 249.03.

Giavalisco, M., Koratkar, A., & Calzetti, D. 1996, ApJ, 466, 831

Hansen, M. & Oh, S. P. 2006, MNRAS, 367, 979

Hayes, M., Östlin, G., & Duval, F. et al. 2014, ApJ, 782, 6

Hayes, M., Östlin, G., & Mas-Hesse, J. M. et al. 2005, A&A, 438, 71

Hayes, M., Östlin, G., & Schaerer, D. et al., 2010, Nature, 464, 562

Hayes, M., Östlin, G., & Schaerer, D. et al. 2013, ApJL, 765, L27

Herenz, E.C., Gruyters, P., & Orlitova, I. et al. 2016, A&A, 587, A78

Kunth, D., Mas-Hesse, J. M., & Terlevich, E. et al. 1998, A&A, 334, 11

Laursen, P., Duval, F., & Östlin, G. 2013, ApJ, 766, 124

Mas-Hesse, J. M., Kunth, D., & Tenorio- Tagle, G. et al. 2003, ApJ, 598, 858

Neufeld, D. A. 1991, ApJL, 370, L85

Östlin, G., Hayes, M., & Duvall, F. et al. 2014, ApJ, 797, 1

Pardy, S. A., Cannon, J. M., & Östlin, G., et al. 2014, ApJ, 794, 2

Reilly, B., Eisner, B., & Cannon, J.M., et.al. 2017. AAS229. 249.03

Rivera-Thorsen, T.E., Hayes, M., & Östlin, G., et al. 2015, ApJ, 805, 1

Scarlata, C., Colbert, J., & Teplitz, H. I. et al. 2009, ApJL, 704, L98

Stark, D. P., Ellis, R. S., Chiu, K., Ouchi, M., & Bunker, A. 2010, MNRAS, 408, 1628

Steidel, C. C., Bogosavljević, M., & Shapley, A. E. et al. 2011, ApJ, 736, 160

Verhamme, A., Schaerer, D., Atek, H., & Tapken, C. 2008, A&A, 491, 89

Zheng, Z., Cen, R., Weinberg, D., Trac, H., & Miralda-Escudé, J. 2011, ApJ, 739, 62

This preprint was prepared with the AAS LaTeX macros v5.2.

5. Tables and Figures

Table 1. Basic Properties of LARS02 and LARS09

Parameter	LARS02	LARS09
Alternate Name	SDSS J090704.88+532656.6	SDSS J090704.88+532656.6
Right ascension (J2000)	$09^{h}\ 07^{m}\ 04.88^{s}$	$08^{h}\ 23^{m}\ 54.96^{s}$
Declination (J2000)	$+53°26'56''$	$+28°06'21''$
Distance (Mpc)	130 [a c]	210 [a c]
z_{opt}	0.030 [b c]	0.047 [b c]

[a]Values derived from luminosity distance.

[b]Derived from SDSS spectroscopy.

[c]From Pardy et al. (2014)

Table 2. Global UV Properties of LARS02 and LARS09[a]

Parameter	LARS02	LARS09
$\mathrm{Mass}_\star$ (10^9 $\mathrm{M}_\odot$)	2.35	51.0
Metallicity (12+log(O/H))	8.23 ± 0.04	8.40 ± 0.05
$\mathrm{L}_{\mathrm{Ly}\alpha}$ (10^{42} cgs)	0.81	0.33
$\mathrm{W}_{\mathrm{Ly}\alpha}$ (Å)	81.7 ± 2.36	3.31 ± 0.28
$f_{\mathrm{esc}}^{\mathrm{Ly}\alpha}$	0.521	0.007
$\mathrm{SFR}_{\mathrm{H}\alpha}$ ($\mathrm{M}_\odot$ yr^{-1})	1.41	40.7
$\mathrm{SFR}_{\mathrm{FUV}}$ ($\mathrm{M}_\odot$ yr^{-1})	1.01	15.0

[a]From Hayes et al. (2014)

Table 3. HI Properties of LARS02 and LARS09

Parameter	LARS02	LARS09
Single-dish S_{HI} (Jy km s^{-1})	0.70 ± 0.07[a]	1.2 ± 0.1[a]
Interferometric D S_{HI} (Jy km s^{-1})	0.36 ± 0.036[a]	0.60 ± 0.060[a]
Interferometric B+C S_{HI} (Jy km s^{-1})	0.62 ± 0.021[b]	0.62 ± 0.057[b]
Single-dish M_{HI} (10^9 $M_\odot$)	2.8 ± 0.3[a]	13 ± 0.1[a]
Interferometric D M_{HI} (10^9 $M_\odot$)	1.4 ± 0.15[a]	6.2 ± 0.62[a]
Interferometric B+C M_{HI} (10^9 $M_\odot$)	2.72 ± 0.29[b]	7.16 ± 0.97[b]

[a]From Pardy et al. (2014)

[b]This work

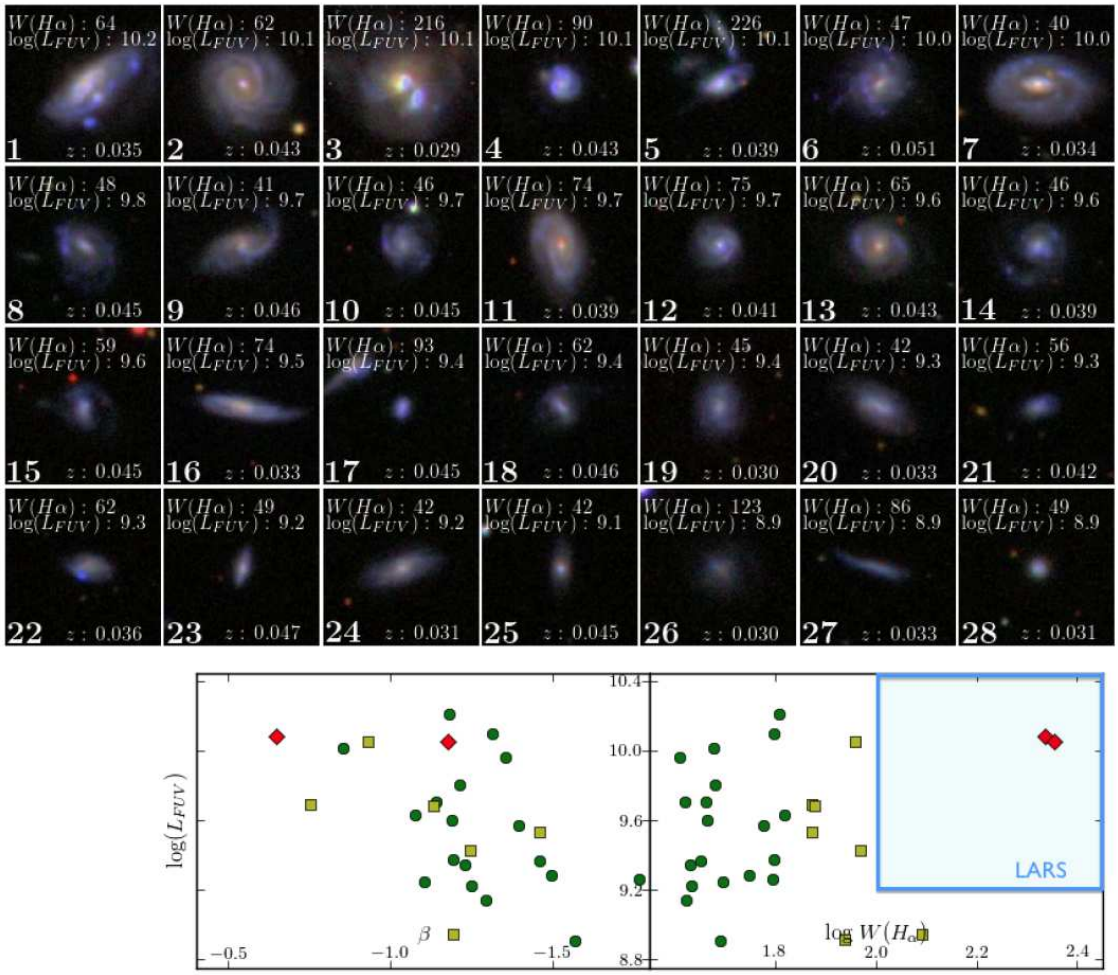

Fig. 1.— Parameters of eLARS galaxies from HST Proposal 1231 (PI: Östlin). Selection of galaxies from the SDSS+GALEX database. Each galaxy is shown by its SDSS thumbnail and in addition to a sequence umber from 1 to 28 shows $W_{H\alpha}$, L_{FUV} and the redshift. The lower panels show the distribution of the sample in the quantities L_{FUV} vs the UV continuum slope (β), and L_{FUV} vs $W_{H\alpha}$. Galaxies with $W_{H\alpha} < 70$Å are shown in green, those with $W_{H\alpha} = 70$ to 140 in yellow, and those with $W_{H\alpha} > 140$Å in red. In the right plot the region occupied by LARS is indicated by a light blue region. The only difference to the original LARS selection is the lower threshold in $W_{H\alpha}$, and only two of the galaxies in the new sample could have been selected by LARS. The two samples complement each other excellently in probing the local population of UV luminous galaxies.

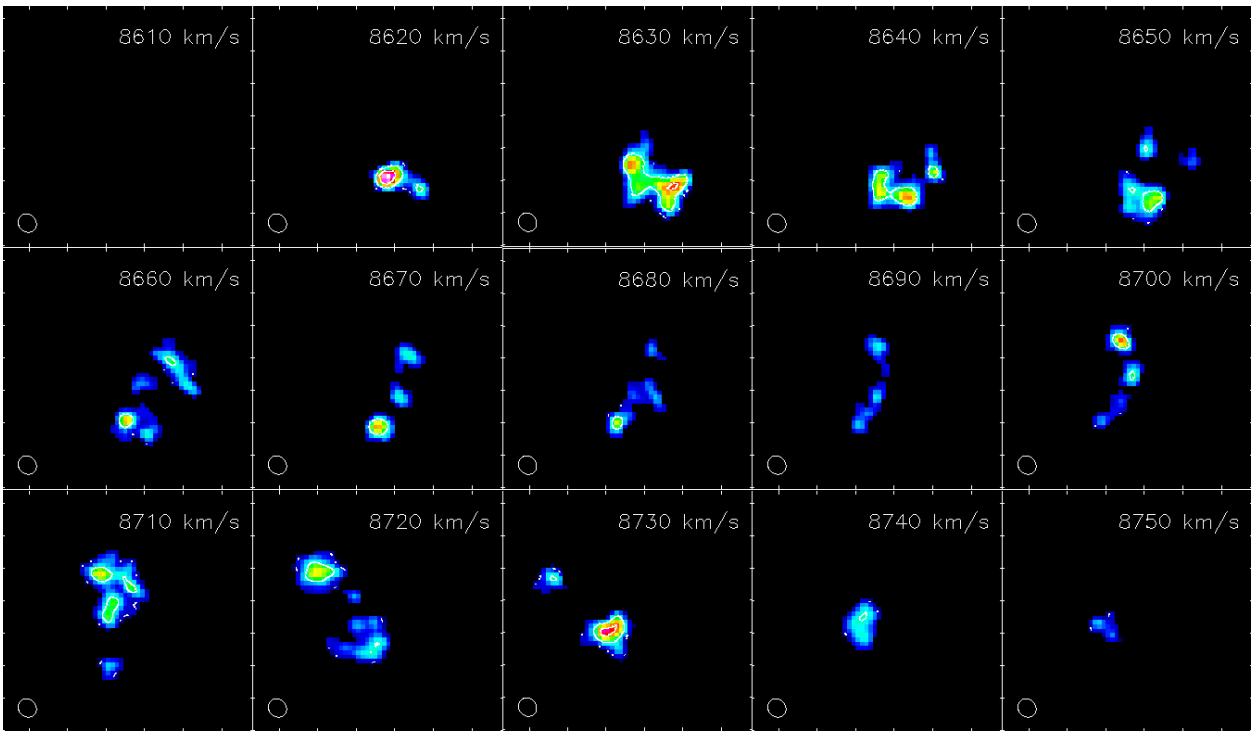

Fig. 2.— Channel map of LARS02. Contours were overlaid at (0.25, 0.5, 0.75, 1) x mJy Bm^{-1}. The beam size is shown in the lower left corner of each channel.

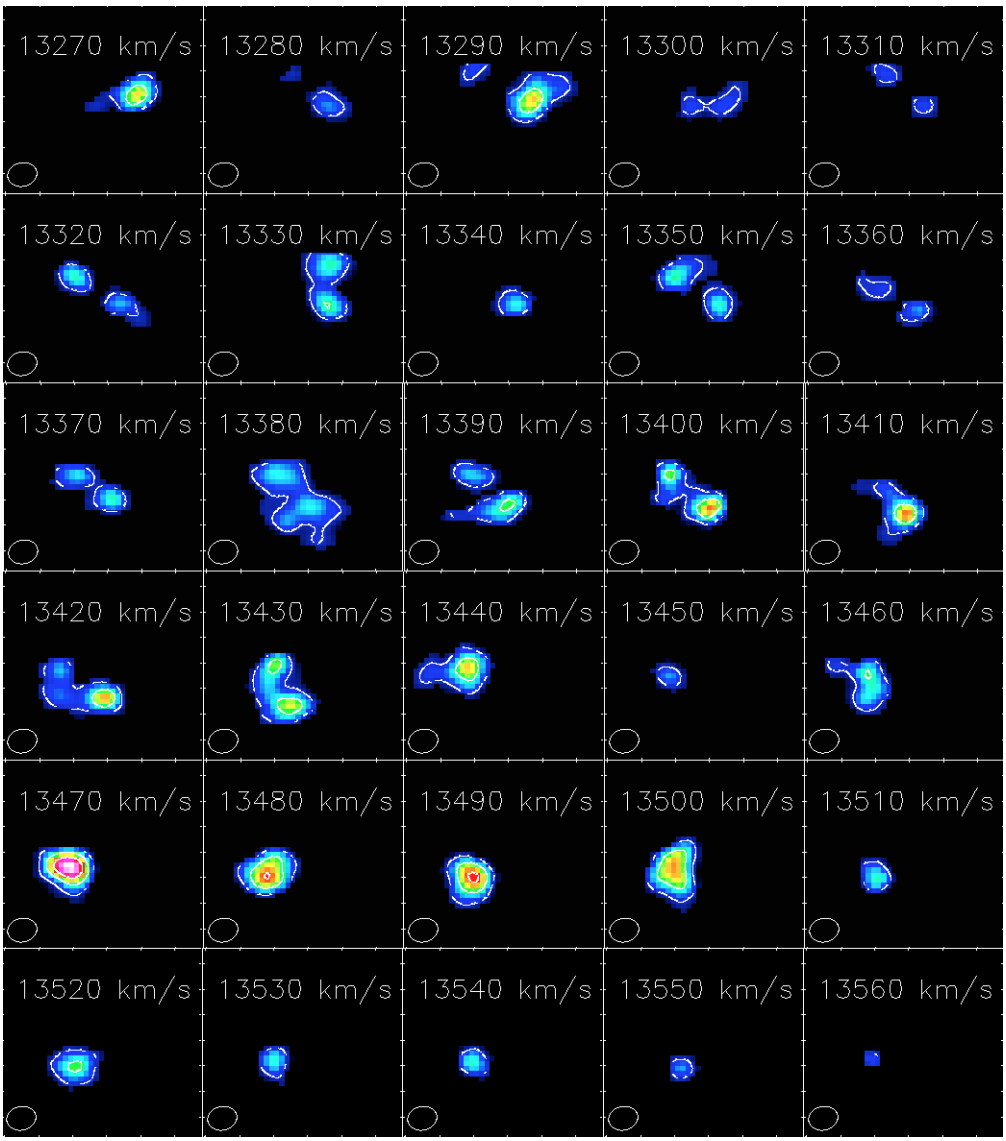

Fig. 3.— Channel map of LARS09. Contours were overlaid at (0.25, 0.5, 0.75, 1) x mJy Bm^{-1}. The beam size is shown in the lower left corner of each channel.

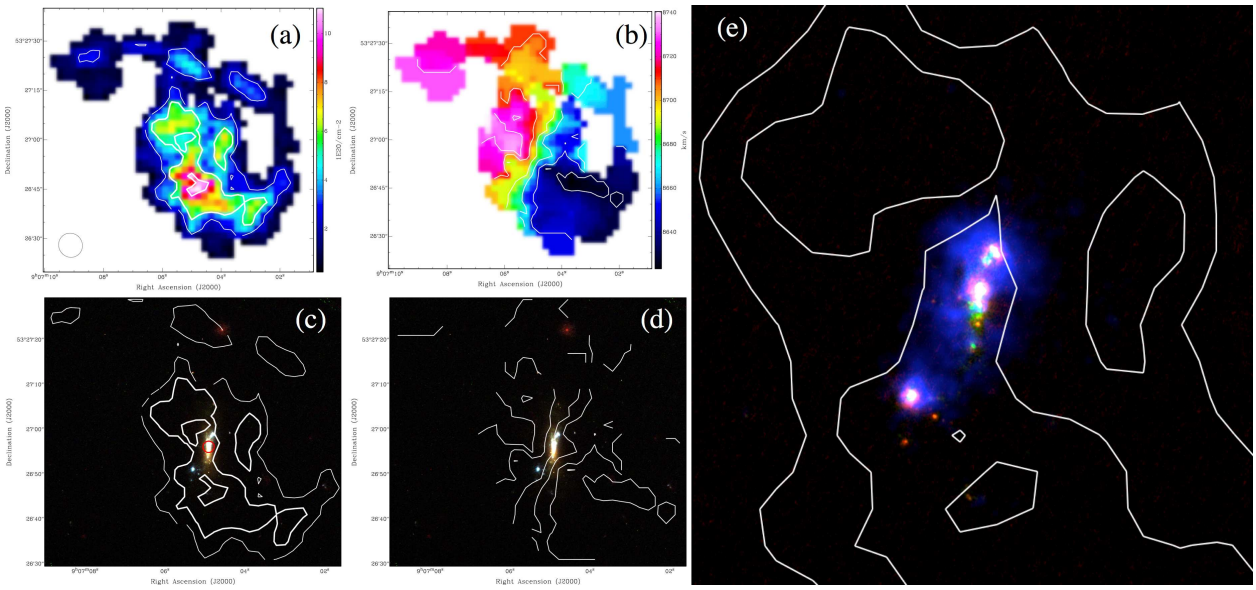

Fig. 4.— VLA B+C configuration HI imaging of the LARS02 system, compared with HST images. (a) shows the HI mass surface density, with column density contours at values of (2.5, 5, 10) x 10^{20} cm^{-2}. (b) shows the intensity-weighted velocity field, with isovelocity contours spanning the range of 8,630 km s^{-1} to 8,730 km s^{-1}, in intervals of 20 km s^{-1} per contour. Panels (c) and (d) show a color HST image, with the same contours as shown in panels (a) and (b) overlaid. Panel (e) shows a false-color HST image of LARS02; red, green, and blue show continuum-subtracted Hα , FUV continuum, and continuum-subtracted Lyα , respectively. The white contours in (e) are the same as in panel (a). The beam size is shown in panel (a). The red circle in panel (c) shows the location of the HST/COS spectroscopic aperture (see Rivera-Thorsen et al. 2015); our HI data accurately constrain the total HI column density along this line of sight. Comparing to the optical morphology, extended HI gas is detected at high significance up to ∼30 kpc from the optical body of LARS02. Note that at D configuration resolution (see Fig. 7), this structure was evident as an extension at high velocities toward the northeast.

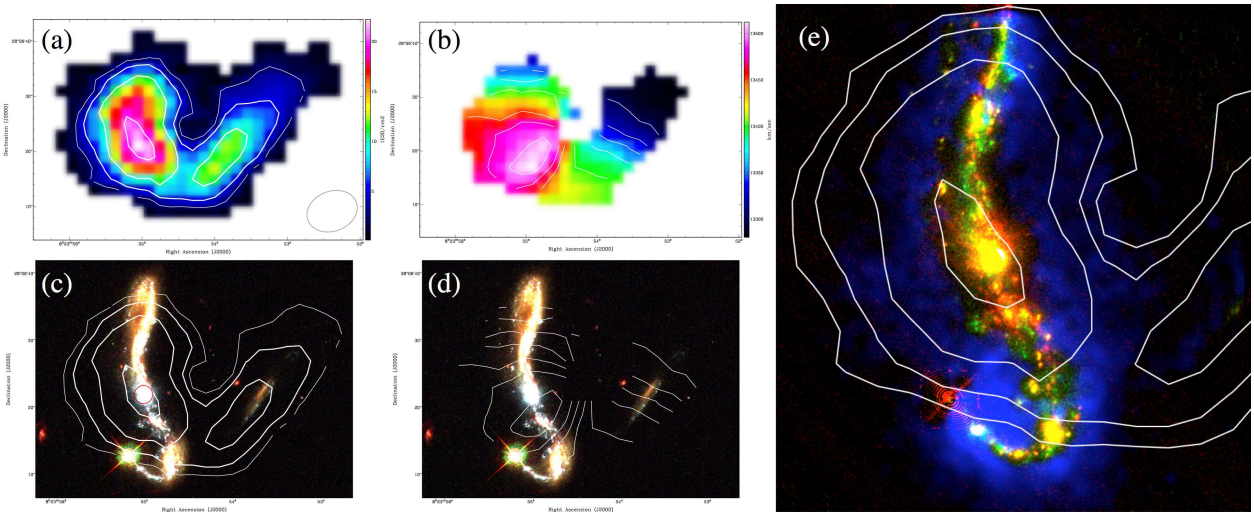

Fig. 5.— VLA B+C configuration HI imaging of the LARS09 system, compared with HST images. (a) shows the HI mass surface density, with column density contours at values of (2.5, 5, 10, 20) x 10^{20} cm^{-2}. (b) shows the intensity-weighted velocity field, with isovelocity contours spanning the range of 13,000 km s^{-1} to 13,500 km s^{-1}, in intervals of 25 km s^{-1} per contour. Panels (c) and (d) show a color HST image, with the same contours as shown in panels (a) and (b) overlaid. Panel (e) shows a false-color HST image of LARS09; red, green, and blue show continuum-subtracted Hα , FUV continuum, and continuum-subtracted Lyα , respectively. The white contours in (e) are the same as in panel (a). The beam size is shown in panel (a). The red circle in panel (c) shows the location of the HST/COS spectroscopic aperture (see Rivera-Thorsen et al. 2015); our HI data accurately constrain the total HI column density along this line of sight. Comparing to the optical morphology, these high-resolution HI data clearly reveal that LARS09 is interacting with the nearby field galaxy SDSSJ0823. Note that at D configuration resolution (see Fig. 8), this interaction was not discernible.

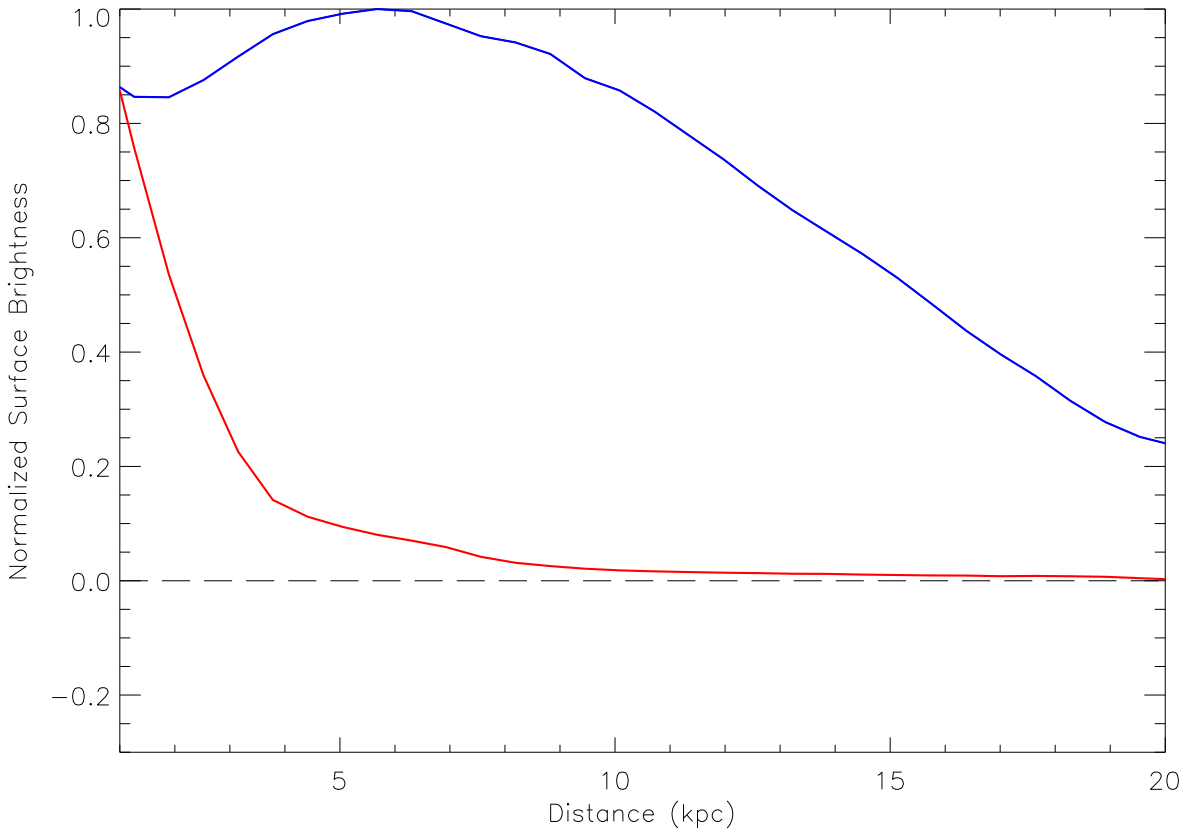

Fig. 6.— Pixel by pixel radial plot of HI and Lyα emission for LARS02. The red line represents the normalized surface brightness of the Lyα emission; the blue line shows the normalized surface brightness of the HI. Because the centers for our annuli were positioned at the center of the Lyα pointing, the emission falls off smoothly. The peak surface brightness of the neutral hydrogen gas, however, was noticeably offset from this position, resulting in an increase in surface brightness before falling away at larger radii.

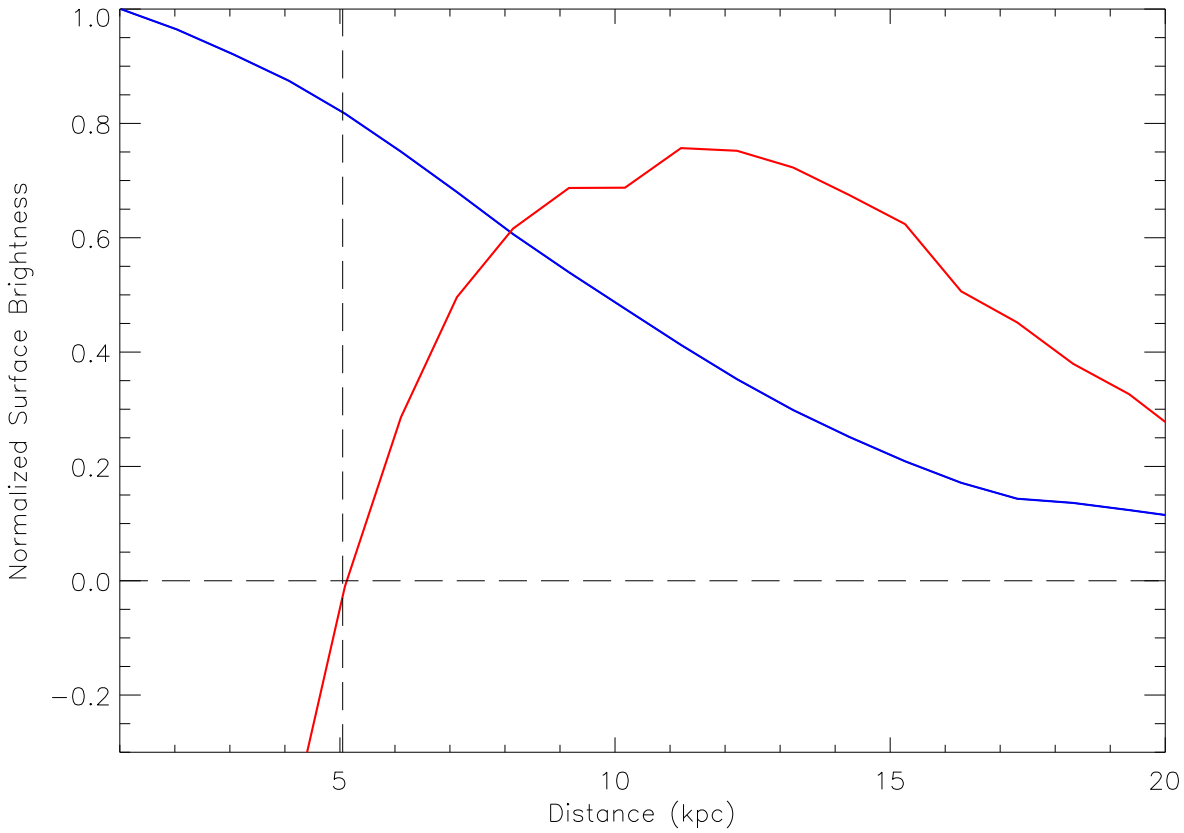

Fig. 7.— Pixel by pixel radial plot of HI and Lyα emission for LARS09. The red line represents the normalized surface brightness of the Lyα emission; the blue line shows the normalized surface brightness of the HI. The horizontal dotted line shows the transition from net Lyα absorption (below) to net Lyα emission (above). The vertical dotted line shows where this transition occurs. The high Lyα surface brightness emission favors regions of low HI mass surface density.

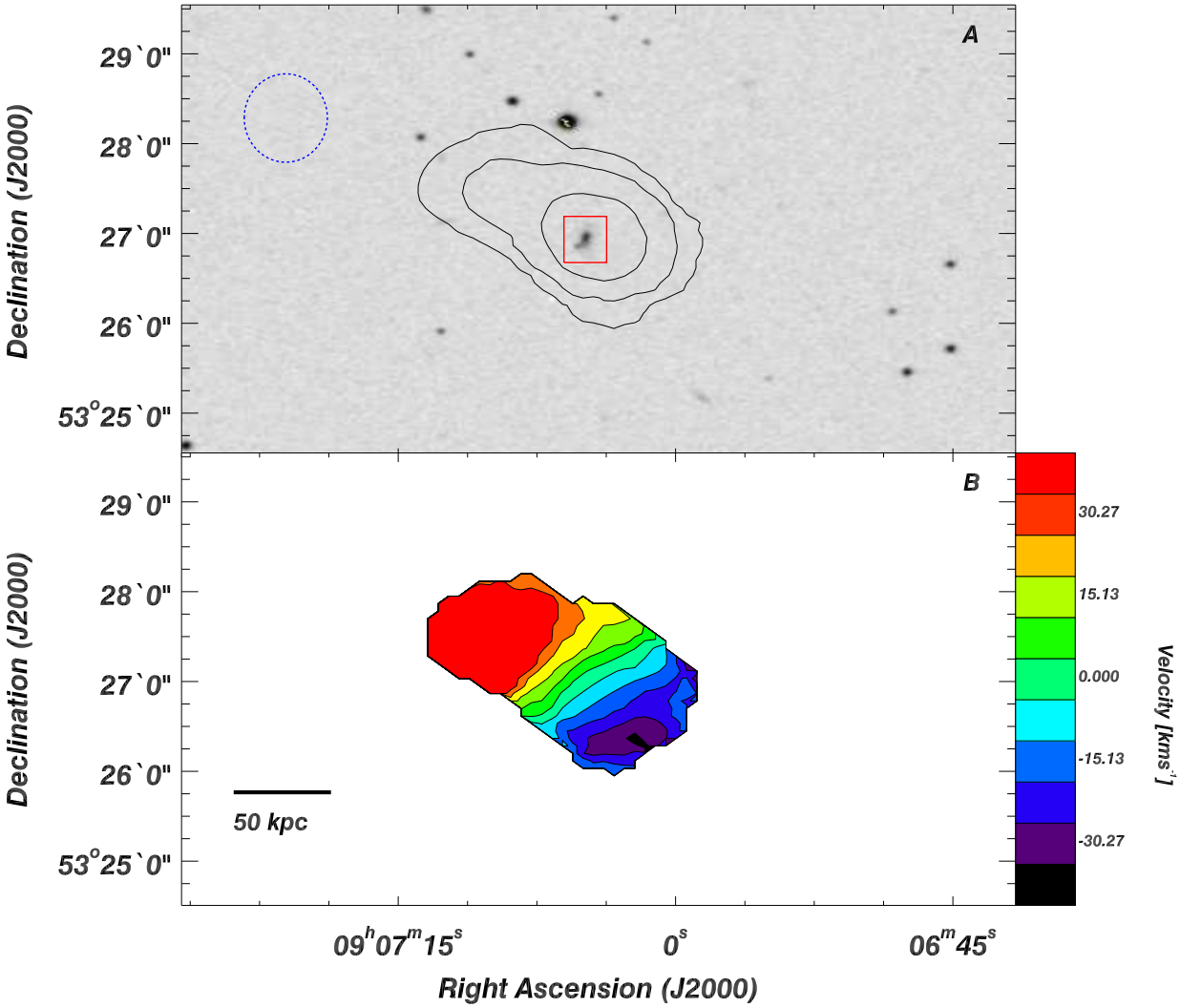

Fig. 8.— HI and optical comparison of LARS02 from Pardy et al. (2014). Panel (a) shows a Digitized Sky Survey image, overlaid with contours of HI surface density at levels of (0.65, 1.3, 2.6, 5.2, 10.4, 20.8) x 10^{19} cm^{-2}. The beam size (59″) is shown in the upper left, and the approximate location and size of the 14 kpc x 14 kpc HST UV imaging is shown by a red square. Panel (b) shows the HI intensity-weighted velocity field.

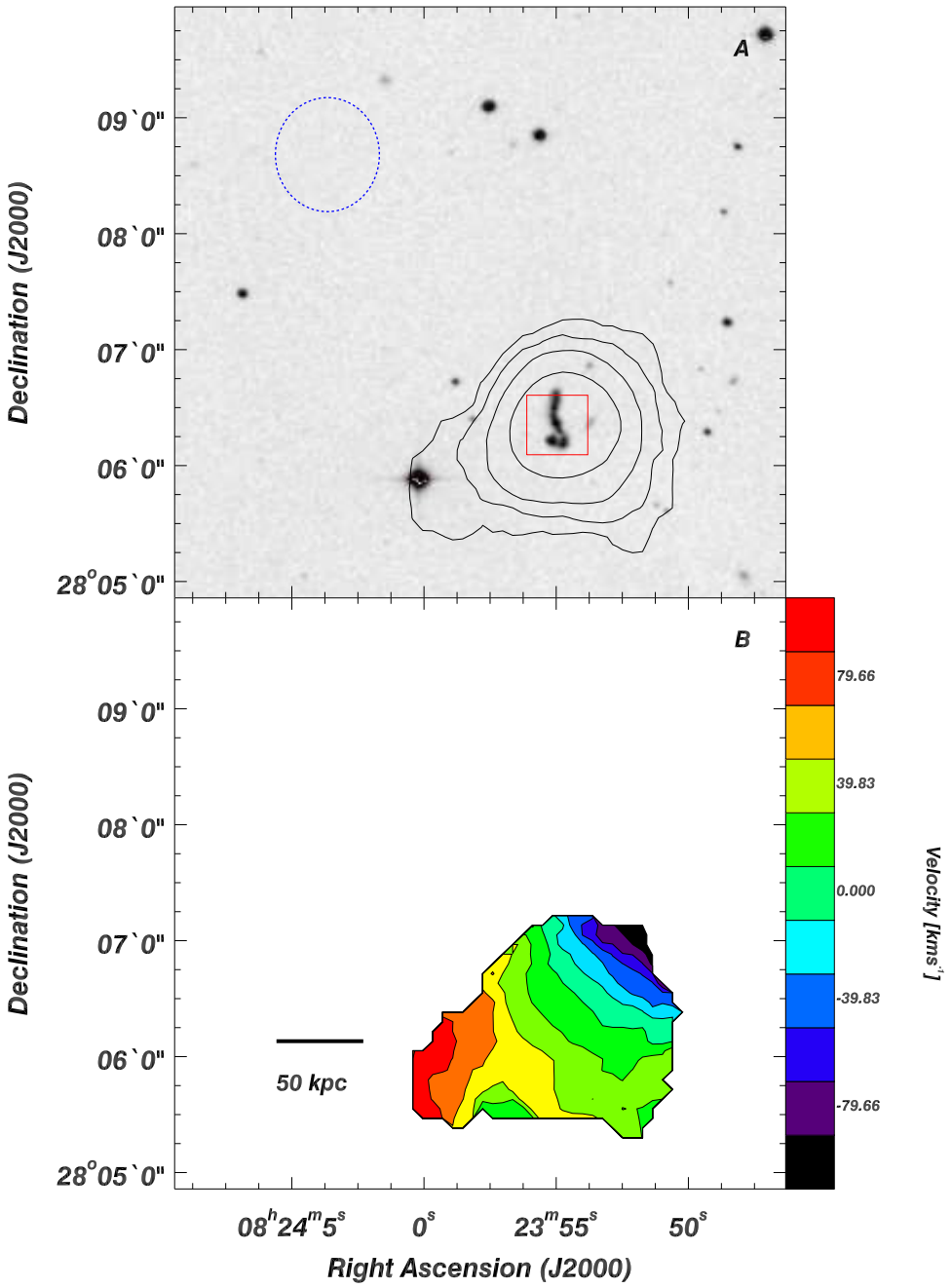

Fig. 9.— HI and optical comparison of LARS09 from Pardy et al. (2014). Panel (a) shows a Digitized Sky Survey image, overlaid with contours of HI surface density at levels of (0.65, 1.3, 2.6, 5.2, 10.4, 20.8) x 10^{19} cm^{-2}. The beam size (59″) is shown in the upper left, and the approximate location and size of the 26 kpc x 26 kpc HST UV imaging is shown by a red square. Panel (b) shows the HI intensity-weighted velocity field.